THE JOURNAL OF PHYSICAL CHEMISTRY C
A JOURNAL OF THE AMERICAN CHEMICAL SOCIETY

pubs.acs.org/JPCC

Article

Two-Body Origin of Recombination-Induced Photocurrent Signals for Drift Velocity Resolution in Perovskite Solar Cells

Saba Mahmoodpour, Zijian Gan, Liang Yan, Wei You, and Andrew M. Moran*

Cite This: https://doi.org/10.1021/acs.jpcc.5c05484

Read Online

ACCESS | Metrics & More | Article Recommendations | Supporting Information

ABSTRACT: Recombination-induced nonlinear photocurrent (NLPC) spectroscopy enables the resolution of nanosecond-scale charge transport in thin-film perovskite photovoltaic cells. In this pump−probe-like method, the first laser pulse initiates carrier drift to the electrodes, while the second pulse probes the transient carrier concentration remaining in the active layer via a saturation effect, wherein carriers excited by separate pulses interact and recombine on the ∼100 ps time scale. The two-body nature of the signal generation mechanism has typically been confirmed through standalone control experiments rather than by characterizing the response alongside the dynamics in a single measurement. Here, we vary both the delay times and laser fluence in NLPC experiments conducted on $MAPbI_3$-based devices to confirm that the nonlinearity originates from two-body recombination processes involving independently excited carrier populations. In addition, a simplified model is introduced to capture the behaviors underlying the responses of $MAPbI_3$ photovoltaic devices while remaining practical for data analysis and interpretation. To place the NLPC results in the context of related methods, our analysis suggests that recombination-induced and higher-order perturbative NLPC-like action spectroscopies provide equivalent time-of-flight information when carrier recombination is fast compared to charge transport across the illuminated region of the active layer. Together, the experiments and modeling framework presented in this work clarify the capabilities and limitations of NLPC spectroscopy for measurements of charge transport in thin-film photovoltaic devices.

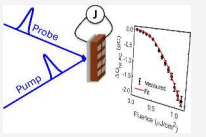

Downloaded via UNIV OF NORTH CAROLINA on November 21, 2025 at 18:34:50 (UTC).
See https://pubs.acs.org/sharingguidelines for options on how to legitimately share published articles.

1. INTRODUCTION

Nonlinear action spectroscopies represent an emerging class of experimental methods that probe spontaneous functional processes initiated by a sequence of laser pulses in systems such as solar cells and biological light-harvesting complexes.[1−11] A key advantage of action spectroscopies is their flexibility: any measurable aspect of the system's response can be leveraged to extract the targeted information. This principle underlies the development of a broad range of nonlinear photocurrent (NLPC) techniques.[2,3,7,9,12−16] For example, phase-sensitive four-pulse action spectroscopies have been employed to probe femtosecond dephasing and charge transfer processes in the active layers of photovoltaic cells.[2−4,12,14] Alternatively, carrier recombination-induced nonlinearities (e.g., device saturation) have been applied to investigate long-range carrier transport with time resolution up to 3 orders of magnitude shorter than that of a conventional time-of-flight approach (e.g., 0.1 ns versus 0.1 μs time scales).[17−21] Inspired by nonlinear optical experiments, our group has also developed NLPC analogues of color-tuned two-dimensional spectroscopies[20−22] and photocurrent-detected transient grating methods based on saturation processes.[23,24] Although carrier recombination can undermine phase-sensitive measurements of femtosecond dynamics, these nonlinearities can provide valuable mechanistic insights when implemented under appropriate conditions.[15,25]

Here, we present NLPC experiments on $MAPbI_3$ photovoltaic cells to confirm the two-body nature of the recombination-induced signal generation mechanism, while simultaneously probing charge transport in the active layer. This approach eliminates the need for separate control experiments to infer the many-body response, thereby reducing ambiguities in the interpretation of carrier drift velocities. Like a traditional time-resolved spectroscopy, NLPC measurements track the concentration of photoexcited carriers in the illuminated region of the active layer as a function of the delay time between two laser pulses.[17−19] However, as illustrated in Figure 1, the action signal reflects the saturation of the time-integrated photocurrent (i.e., the total amount of collected charge) arising from interactions between carriers excited by separate pulses. While the origin of the many-body nonlinearity can be obscured in fixed-fluence experiments, the present measurements vary the excitation intensity to resolve the nonlinear dependence of the recombination-induced saturation curve at each delay point. The signals are interpreted with a simplified algebraic model that captures essential features of the response and permits direct least-squares fitting of experimental data. This modeling approach provides intuitive insight into the signal's sensitivity to carrier transport, with the broader goal of revealing the two-body origin of the nonlinearity.

Received: August 5, 2025
Revised: November 2, 2025
Accepted: November 3, 2025

ACS Publications

© XXXX American Chemical Society

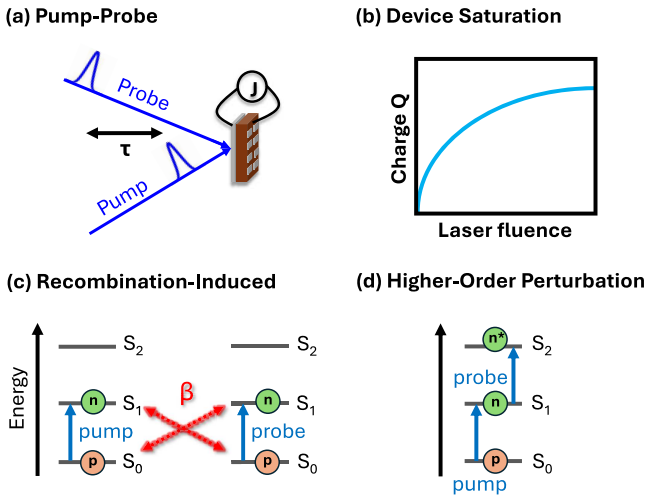

Figure 1. Recombination-induced nonlinear photocurrent response for a sequence of two laser pulses. (a) NLPC measurements share characteristics with conventional pump−probe techniques. (b) The amount of charge extracted from a photovoltaic device saturates as the laser fluence increases due to carrier recombination. (c) The two laser pulses excite independent populations of electrons and holes, which interact and recombine to saturate the photovoltaic device. (d) In higher-order perturbative responses, both pulses interact with the same carriers, enabling transitions among excited states.

Recombination-induced NLPC responses provide time-resolved information on carrier transport that is otherwise inaccessible in single-pulse experiments without resorting to conventional time-of-flight detection.[26,27] As discussed in our prior work,[19] this aspect of NLPC signal generation distinguishes it from cascades of lower-order nonlinearities encountered in higher-order Raman spectroscopies under off-resonant conditions.[28−32] For instance, nonlinear optical cascades can obscure the detection of two-dimensional (2D) Raman signals, where vibrational coherences evolve along two controlled delay times.[30−32] In cascaded artifacts, the lower-order Raman responses combine to mimic a higher-order 2D spectrum yet fail to reveal mode couplings or anharmonicities beyond what is captured in a conventional one-dimensional Raman spectrum. A similar challenge arises in phase-sensitive NLPC experiments targeting femtosecond dynamics, where recombination-induced responses can overwhelm the desired coherent signals.[33−36] Recombination processes involving carriers excited by separate laser pulses are termed "incoherent mixing" and have been likened to cascades due to their capacity to obscure meaningful dynamics in NLPC-like experiments based on higher-order perturbative responses.[9]

As indicated in Figure 1c, the two laser pulses excite independent charge carrier populations to singly excited states, which subsequently saturate the response of the photovoltaic cell on the 100 ps time scale in the recombination-induced NLPC technique.[17−19] In contrast, sequences of laser pulses interact with the same carriers in higher-order perturbative nonlinear responses, enabling transitions among excited states (see Figure 1d).[3,4,13] Like multidimensional spectroscopies conducted with optical detection, higher-order perturbative NLPC-like techniques can similarly employ sequences of phase-locked pulses to reveal femtosecond correlations between the pumped and probed resonances.[2−4,12,14] Although femtosecond time resolution and correlated line broadening are inaccessible with recombination-induced nonlinear responses, this approach yields signatures of long-range carrier transport in the experimentally controlled delay time. To clarify the relationship between the two experimental approaches, we further extend our model below to show that recombination-induced and higher-order perturbative NLPC-like techniques provide indistinguishable time-of-flight information under certain limiting conditions.

2. EXPERIMENTAL METHODS

2.1. Device Fabrication. Patterned indium-doped tin oxide (ITO) glass substrates (Thin Film Devices, Inc.; 20 Ω/square) were cleaned by ultrasonic treatment in deionized water, acetone, and 2-propanol (15 min each). After drying under a nitrogen stream, the substrates were exposed to UV−ozone for 15 min. All subsequent spin-coating steps were performed inside a nitrogen-filled glovebox. A solution of PTAA (poly(triarylamine), Sigma-Aldrich) in toluene (2 mg/mL) was spin-coated onto the cleaned ITO substrates at 4000 rpm for 30 s, followed by baking at 100 °C for 10 min. After the mixture was cooled to room temperature, a $MAPbI_3$ perovskite precursor solution was deposited onto the PTAA layer.

The perovskite precursor solution was prepared by dissolving PbI_2 and MAI in a DMF/DMSO (9:1 v/v) solvent mixture at a Pb^{2+} concentration of 0.8 M. Prior to perovskite deposition, the PTAA layer was prewetted by spin-coating pure DMF twice at 2000 rpm for 3 s each. The $MAPbI_3$ solution was spin-coated in a two-step process: 2000 rpm for 2 s, followed by 4000 rpm for 20 s. At 8 s into the second step, 0.3 mL of toluene was drop-cast onto the spinning substrate. The film was then annealed at 65 °C for 10 min and subsequently at 100 °C for 10 min. All perovskite processing was conducted in a nitrogen-filled glovebox. After being cooled, the perovskite-coated substrates were transferred to a second nitrogen-filled glovebox.

To complete the device fabrication process, 50 nm of C_{60}, 5 nm of BCP (bathocuproine), and 80 nm of copper were thermally evaporated at a base pressure of 3×10^{-7} Torr. The active area (0.13 cm^2) was defined by using a shadow mask. Device characterization was performed under AM 1.5 G illumination at an intensity of 100 mW/cm^2, provided by a 300 W Oriel 91160 solar simulator calibrated with an NREL-certified standard silicon reference cell. Current density−voltage ($J-V$) curves were recorded using a Keithley 2400 digital source meter with a scan rate of 0.05 V/s. The thicknesses of the active layers ranged from 175 to 200 nm with an average of 190 nm, as determined by scanning electron microscopy.

2.2. NLPC Experiments. The NLPC experiments presented here utilized a PicoQuant diode laser system, as described in prior publications.[18,23] Two LDH-P-C-405 diode lasers independently generated 400 nm laser pulses with durations of 40 ps and energies of 100 pJ. The time delay between pulses was controlled with a minimum step size of 24 ps using a PicoQuant SEPIA II SOM 828-D oscillator module. The two laser beams were directed to the photovoltaic cell and focused to full width at half-maximum (fwhm) spot sizes of 80 μm at the plane of the active layer, where the laser fluences ranged from 0.18 to 1.2 $\mu J/cm^2$.

The diode lasers were operated at 5 kHz to allow the signal baseline to re-establish during the 200 μs interval between laser shots. Both the recovery of the initial device conditions and the response time of the detection electronics are considered in

https://doi.org/10.1021/acs.jpcc.5c05484
J. Phys. Chem. C XXXX, XXX, XXX−XXX

determining the overall data acquisition rate. Carrier drift typically removed all photoexcited species from the active layers of the $MAPbI_3$ devices within ~1 μs after photoexcitation. In addition, the Stanford Research Systems SR570 current amplifier used for signal detection broadened the resulting current pulses to approximately 20 μs, which ultimately determined the maximum repetition rate used in these experiments.

Like earlier two-pulse NLPC experiments,[17−21] the signals were acquired with a sequence of four conditions: pulses 1 and 2 on $(Q_{1+2}(\tau))$, pulse 1 on (Q_1), pulse 2 on (Q_2), and both pulses off (Q_0).[19−22] To cycle through the four conditions, the individual laser beams were turned on and off by using LabVIEW software interfaced with the PicoQuant control system. The signal, $\Delta Q_{NLPC}(\tau) = Q_{1+2}(\tau) - Q_1 - Q_2 + Q_0$, represents the component of device saturation induced by recombination processes involving carriers photoexcited by separate pulses. The signal-to-noise ratio was optimized by cycling through the four pulse sequences, 15 laser fluences, and 36 delay points. Repeating the full set of conditions five times and averaging the data results in a data acquisition time of 1 h. Signals were monitored during the experiments to confirm the stabilities of the devices.[23]

The total amount of charge produced by a device was determined by time-integrating the amplified photocurrent. The photocurrent pulses were broadened to approximately 20 μs with the 2-μA/V sensitivity and gain mode (low noise) settings of the Stanford Research Systems SR570 current amplifier employed in the present measurements. Signals were processed by using a National Instruments NI USB-6361 data acquisition board with a 1 MHz sampling rate, corresponding to an interval of 1 μs between points. The total amount of charge collected from a device was computed by multiplying the time-integrated voltage output by the current-to-voltage amplification factor.

3. NLPC SIGNAL GENERATION MECHANISM

To address the limitations of prior finite-differencing approaches,[18,19] the present model for simulating NLPC spectroscopy reduces computational cost while retaining essential physical behaviors, making it well-suited for least-squares fitting and data interpretation. The fundamental concepts underlying the signal generation mechanism are first introduced through a qualitative discussion of time-of-flight principles. Simplified expressions for the signals are then derived to ensure consistency with the experimental signatures of carrier drift velocity dispersion.

3.1. Fundamental Aspects of Nonlinearity. The NLPC technique involves a pair of incident laser pulses with a variable delay time, like a conventional pump−probe experiment; however, the detection process is mediated by interactions between separate carrier populations, as illustrated in Figure 2. The first laser pulse initiates charge transport by exciting charge carriers near the transparent ITO contact. Under the influence of the internal electric field, the electrons (n_1) traverse the full thickness of the active layer toward the copper electrode, while the holes (p_1) are directly collected by the ITO electrode (see Figure 2b). The concentration of photoexcited carriers remaining in the photoexcited region of the active layer is subsequently probed at the delay time, τ, by using a second laser pulse. Although the second pulse does not directly interact with p_1 and n_1, it generates an additional population of carriers, p_2 and n_2, that undergo mutual

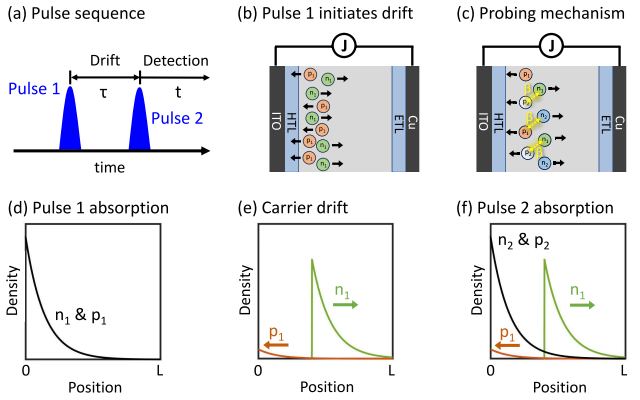

Figure 2. Overview of NLPC signal generation mechanism. (a) Pulses 1 and 2 are separated by an experimentally controlled delay time τ, while the response of the device saturates on the ~100 ps time scale during t. (b) Absorption of the first pulse initiates drift of electrons and holes. (c) Two-body recombination processes involving carriers photoexcited by separate pulses saturate the response of the device. (d) The initial carrier density generated by absorption of pulse 1 decays exponentially with position near the transparent ITO electrode. (e) Electrons and holes drift in opposite directions during the delay period. (f) The magnitude of the NLPC signal reflects the delay-dependent spatial overlap of the carrier distributions excited by the two laser pulses.

recombination with those from the first pulse. These recombination processes, occurring between carriers photoexcited by separate pulses, saturate the photocurrent on the ~100 ps time scale,[17−19] enabling the resolution of long-range transport within the active layers of photovoltaic cells (see Figure 2c). At sufficiently low fluences, NLPC signals scale linearly with both p_1 and n_1 due to the dominance of two-body recombination processes, including both radiative recombination and nonradiative Shockley−Read−Hall mechanisms.[37,38]

Although the carrier densities generally broaden while traversing the active layer due to numerous cycles of capture and release at shallow trap sites,[39−41] it is shown in Section 3.2 that the NLPC signal profiles are largely insensitive to the exact shapes of these distributions, because (i) dispersion is negligible for the hole density due to efficient injection into the adjacent HTL, (ii) broadening of the electron density is minimal over the length scale of the optical penetration depth, and (iii) the photocurrent is integrated over time to yield the net collected charge.[18,19] Therefore, in the simplified numerical model developed in Section 3.3, we assume that the carrier densities retain their one-sided exponential shapes while drifting across the active layer, as depicted in Figure 2d−f. The densities excited by the first laser pulse drift away from the photoexcited region of the device during the experimentally controlled delay time, whereas the second pulse tracks the residual carrier concentration. For illustration, the transit time across this area is typically 7 ns for $MAPbI_3$ thin-film devices with drift velocities near 5 m/s and light penetration depths of 35 nm, corresponding to absorption of 400 nm laser pulses.[18] Because carrier drift is slow compared to the 100 ps time scale of device saturation, the probing mechanism is localized to the portion of the active layer adjacent to the ITO contact in $MAPbI_3$ photovoltaic cells.

3.2. Drift Velocity Dispersion in Time-of-Flight Measurements. While carrier density distributions can broaden significantly during transit across the active layers of

https://doi.org/10.1021/acs.jpcc.5c05484
J. Phys. Chem. C XXXX, XXX, XXX−XXX

thin-film devices, the sensitivity of NLPC measurements to such dispersive effects depends on the optical penetration depth.[18] Here, we provide background information on drift-velocity dispersion mechanisms and the factors that determine their signatures in NLPC measurements. This context motivates the approximations adopted in the simplified model presented in Section 3.3.

Models that incorporate repeated carrier trapping and release from traps have proven effective in explaining signatures of drift-velocity dispersion observed in conventional time-of-flight experiments.[26,39−46] Following light absorption, carriers initially exhibit a trap-free drift velocity determined by the product of the electric field and the intrinsic mobility. However, the effective velocity of the ensemble decreases during transit across the active layer, as carriers are temporarily localized in trap states. The time-dependent mobility measured in conventional time-of-flight experiments, $\mu_{TOF}(t)$, can therefore be related to the intrinsic mobility, μ_0, through the ratio of free to total carriers:[26,39,40]

$$\mu_{TOF}(t) = \mu_0 \frac{N_{free}(t)}{N_{free}(t) + N_{trap}(t)} \quad (1)$$

where $N_{free}(t)$ and $N_{trap}(t)$ denote the mobile and trapped carrier populations, respectively. Free electrons and holes drift within extended states above or below the mobility edges of the conduction and valence bands, whereas multiple-trapping processes slow the average drift velocity and broaden the spatial charge distribution.

NLPC experiments previously conducted on perovskite films are consistent with the predictions of conventional time-of-flight models;[19−21] however, NLPC measurements are uniquely capable of revealing "instantaneous" carrier mobilities with picosecond time resolution by periodically cycling the external bias applied to a photovoltaic cell.[19] To detect velocity deceleration and density broadening, we have additionally conducted NLPC experiments with both co- and counter-propagating pump and probe laser pulses to investigate the dynamics near the ITO and copper electrodes, thereby revealing the ∼100 nm length scale over which drift-velocity dispersion accumulates in $MAPbI_3$.[18] Photocurrent-detected transient grating measurements show similar dispersive effects on carrier diffusion,[23,24] as predicted by related transport models.[39,40,47] Although the multiple-trapping approach primarily focuses on trap characteristics, our prior works suggest that grain boundaries, lattice thermal motions, and the organic matrix all contribute to dispersive transport. Therefore, we find that the data are well described by phenomenological models that incorporate a more general, inhomogeneous distribution of carrier transit times.[23,24]

To illustrate the effects of dispersive transport on the shape of the carrier density, we simulate the dynamics in electron and hole distributions using a multiple-trapping model in Figure 3. Because this approach has been fully described elsewhere, the algorithm for simulating the density distribution is summarized in the Supporting Information. The initial velocity is set equal to a typical value of 5 m/s for our $MAPbI_3$ devices.[19−21,23] In addition, the characteristic energy of the exponential shallow-trap distribution is given by 50 meV,[48−50] while the deepest trap level is set to 0.4 eV.[51−53] Carrier release from trap states correspond to an Arrhenius-activated process in which the average time interval between successive attempts to overcome the energy barrier is 1 ps.[21,26,39] Importantly, the conclusions

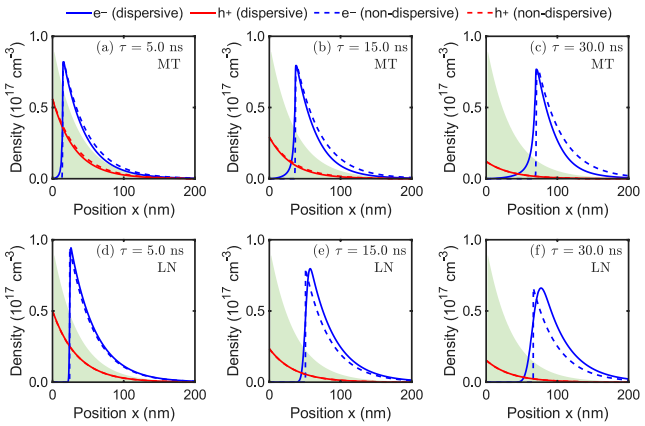

Figure 3. Drift velocity dispersion in $MAPbI_3$ films is simulated using two models, wherein x = 0 and 200 nm correspond to interfaces with the HTL and ETL layers, respectively. Panels (a)−(c) depict results from a conventional multiple-trapping model, while panels (d)−(f) employ a phenomenological approach based on a log-normal distribution of trapping time scales. In each case, the solid lines represent carrier densities incorporating dispersive effects, and one-sided exponential profiles are overlaid to illustrate reshaping of the distributions during transit.

drawn here are insensitive to variations in these parameters within physically reasonable ranges as minimal dispersion is accumulated on the length scale of the light penetration depth.

The multiple-trapping simulations shown in Figure 3a−c indicate that drift velocity dispersion gradually accumulates as the electron density drifts away from the illuminated region of the active layer toward the ETL and copper electrode (x = 200 nm in Figure 3). In contrast, the effects of dispersion on the hole distribution are negligible due to light absorption and short-range drift into the adjacent HTL layer (x = 0 nm in Figure 3). One-sided exponential distributions (dashed line) are overlaid with the densities generated via the multiple-trapping approach (solid line) to illustrate the length scale over which dispersive distortions in the electron density emerge. Because the recombination processes underlying the nonlinear response of the device are fast compared to carrier drift, the NLPC signal generation mechanism is concentrated near the transparent electrode. With the 400 nm laser pulses, the exponential light penetration depth in $MAPbI_3$ is only ∼35 nm, making the experimental measurements largely insensitive to broadening of both the hole and electron densities.

Because drift velocity dispersion can originate from traps, grain boundaries, and thermal fluctuations in the lattice, we have simulated the processes with a phenomenological model based on a general inhomogeneous distribution of transit times. This approach captures the essence of the multiple-trapping approach without delineating the contributions from the specific processes that induce dispersion. Light absorption first produces an exponential distribution of carrier density in the active layer at t = 0:

$$\rho(x, t = 0) = \rho_0 \exp(-\alpha x) \quad (2)$$

where ρ_0 is the carrier density at the interface with the active layer and α is the absorption coefficient at the wavelength of the incident laser pulse. Although multiple-trapping models predict a power-law decay in the drift velocity,[39−41] we find that the effect is readily captured by assuming distinct "free"

https://doi.org/10.1021/acs.jpcc.5c05484
J. Phys. Chem. C XXXX, XXX, XXX−XXX

and "trap-limited" phases of transport with an exponential onset:[18,19,24]

$$v_d(t, t_{trap}) = v_{free} \exp(-t/t_{trap}) + v_{trap}[1 - \exp(-t/t_{trap})] \quad (3)$$

where t_{trap} is the time scale of trap-induced deceleration in carrier drift. The displacement of the carrier density from the initial position at the ITO interface is then expressed as[18,24]

$$x_d(t, t_{trap}) = \int_0^t v_d(t', t_{trap})\, dt' = t_{trap}(v_{free} - v_{trap}) [1 - \exp(-t/t_{trap})] + v_{trap}t \quad (4)$$

Dispersive broadening can then be incorporated into the hole and electron densities using[24]

$$p_1(x, t) = \frac{1}{\xi_{trap}\sqrt{2\pi}} \int_0^\infty t_{trap}^{-1} \exp\left\{-\frac{[\ln(t_{trap}) - \ln(\overline{t}_{trap})]^2}{2\xi_{trap}^2}\right\} \rho(x - x_d(t, t_{trap}), t)\, dt_{trap} \quad (5)$$

and

$$n_1(x, t) = \frac{1}{\xi_{trap}\sqrt{2\pi}} \int_0^\infty t_{trap}^{-1} \exp\left\{-\frac{[\ln(t_{trap}) - \ln(\overline{t}_{trap})]^2}{2\xi_{trap}^2}\right\} \rho(x + x_d(t, t_{trap}), t)\, dt_{trap} \quad (6)$$

Although Gaussian distributions of trapping times were employed in previous work,[23] the log-normal distributions were shown to better approximate the effects of drift velocity dispersion predicted by finite-difference schemes.[18,19,23,24]

The carrier densities shown in Figure 3d–f are computed using eqs 5 and 6, where the mean trapping time $\overline{t}_{trap}$ and width ξ_{trap} are 10 ns and 0.15, respectively. These are typical parameters for our $MAPbI_3$ films.[18,19,23,24] In comparison to the multiple-trapping approach, the fronts of the carrier densities display slightly greater broadening, whereas the trailing edge decays more steeply. Both methods predict similar amounts of carrier density broadening on the 100 nm length scale with only minor dispersive effects on the length scale of the 35 nm light penetration depth. Additionally, hole-density broadening is negligible in all calculations. Notably, these numerical results are consistent with NLPC experiments conducted with both co- and counterpropagating 400 nm laser pulses[18] as well as NLPC measurements of instantaneous mobilities conducted using longer wavelengths.[19]

In the Supporting Information, we employ the standard small-ξ_{trap} expansion of $n_1(x,t)$ to define the following physical regime in which density broadening can be neglected in simulations of NLPC signals:[54]

$$\xi_{trap} \ll \frac{3.8}{\alpha \overline{t}_{trap}(v_{free} - v_{trap})} \quad (7)$$

The right side of eq 7 is ~2.6 given the light penetration depth (α^{-1}) of 35 nm, the difference between initial and final velocities ($v_{free} - v_{trap}$) of 5 nm/ns, and the characteristic time scale of deceleration in carrier drift for $MAPbI_3$ films ($\overline{t}_{trap}$) of 10 ns. This confirms that dispersive broadening of the carrier density is negligible for the empirical value of $\xi_{trap} \approx 0.15$. While eq 7 applies to broadening on the time scale of $\overline{t}_{trap}$, the long-time limit is given by

$$\xi_{trap} \ll \frac{1}{\alpha \overline{t}_{trap}(v_{free} - v_{trap})} \quad (8)$$

The right side of the equation is equal to ~0.7 given the same parameters, reflecting additional accumulation of drift-velocity dispersion. NLPC experiments are largely immune to these effects, because the density is probed only in the region of the active layer near the transparent electrode, and the photocurrent is integrated after processing by the current amplifier to obtain the total amount of charge. In this respect, NLPC differs fundamentally from conventional one-pulse time-of-flight measurements, where density broadening is imprinted on the line shape of the photocurrent measured at an acceptor electrode.[55]

3.3. Simplified Model for Recombination-Induced NLPC Measurements. We next obtain a simplified expression for NLPC signals under the assumptions of a negligible dispersive broadening of the carrier distributions and a single effective trapping time t_{trap}. The initial densities of the holes and electrons, $p_j(x,t)$ and $n_j(x,t)$, generated by the laser pulse are given by

$$p_j(x, 0) = n_j(x, 0) = \frac{f\alpha}{\hbar\omega} \exp(-\alpha x) \quad (9)$$

where f is the laser fluence, ω is the laser frequency, and α is the absorption coefficient of the active layer. Although the two laser beams employed in our experiments have the same frequencies and fluences, the index, j, is included to account for the timing of the pulses. The recombination dynamics of the carrier densities are modeled by solving a pair of coupled differential equations:

$$\frac{\partial p_j(x, t)}{\partial t} = -\beta p_j(x, t) n_j(x, t) \quad (10)$$

and

$$\frac{\partial n_j(x, t)}{\partial t} = -\beta p_j(x, t) n_j(x, t) \quad (11)$$

where β is the overall two-body recombination coefficient accounting for the combined effects of radiative and nonradiative recombination processes.[18,19] Since the carrier drift velocity is on the order of 5 m/s, we assume that the distributions are effectively static on the time scale of device saturation, making the solutions to eqs 10 and 11 valid point-by-point along the x-axis. As a result, the carrier concentrations are reduced to half of their initial values at the characteristic time:

$$t_{1/2} = \frac{1}{\beta\sqrt{p_0 n_0}} = \frac{1}{\beta p_0} = \frac{1}{\beta n_0} \quad (12)$$

where the hole and electron densities at the interface with ITO are denoted as

$$p_0 = n_0 = \frac{\alpha f}{\hbar\omega} \quad (13)$$

For example, a recombination time of $t_{1/2}$ = 99 ps is computed with $\beta = 1.4 \times 10^{-8}$ cm^3/s and $p_0 = n_0 = 7.2 \times 10^{17}$ cm^{-3},

https://doi.org/10.1021/acs.jpcc.5c05484
J. Phys. Chem. C XXXX, XXX, XXX−XXX

Table 1. Parameters of NLPC Model

$\frac{f\alpha(\omega_j)}{\hbar\omega_j}$	f	α^{-1}[a]	$\hbar\omega$	β[b]	A
7.2×10^{17} cm^{-3}	1.22 μJ/cm^2	34 nm	3.10 eV	1.4×10^{-8} cm^3/s	5027 μm^2

[a]Absorbance coefficient for $MAPbI_3$ from ref 56. [b]Overall two-body recombination coefficient for $MAPbI_3$ from ref 57.

where the parameters used to compute the density are given in Table 1.

The rates of trap-assisted Auger recombination processes similarly exhibit a quadratic scaling of the rate with respect to the incident laser fluence.[38] In this process, two photoexcited carriers interact with a third carrier that is already located at a trap site before the laser pulse arrives. To compete with two-body recombination processes, the density of occupied trap states must be comparable to the photoexcited carrier density on the order of 7×10^{17} cm^{-3}. Although estimates of trap densities in $MAPbI_3$ films are generally lower (10^{14}–10^{16} cm^{-3}),[49,58−60] contributions from trap-assisted Auger processes cannot be entirely ruled out. For instance, quadratic scaling behaviors attributed to defect-mediated Auger recombination have been reported in other semiconductors, such as MoS_2, where deep trap states contribute to nonradiative carrier annihilation.[61] Importantly, these Auger processes involve a background of immobilized (pre-existing) charge carriers and therefore do not prohibit measurements of carrier drift dynamics.

Because the parameter regime defined in eq 7 is satisfied for the present experiments, carrier transport is modeled under the assumption that the carrier densities maintain their one-sided exponential profiles during transit across the photoexcited region of the active layer:

$$p_1(x, \tau) = p_0 \exp[-\alpha x - \alpha x_d(\tau)] \tag{14}$$

and

$$n_1(x, \tau) = n_0 \theta[x - x_d(\tau)] \exp[-\alpha x + \alpha x_d(\tau)] \tag{15}$$

where $\theta[x - x_d(\tau)]$ is a Heaviside step function. After absorption of an individual laser pulse, the amount of charge collected from the photovoltaic device can be expressed as

$$Q_j = e{\cdot}A{\cdot}\int_0^L \{p_j(x, 0) + n_j(x, 0) - \beta{\cdot}t_{1/2}{\cdot} p_j(x, 0)n_j(x, 0)\}\,dx \tag{16}$$

where e is the elementary charge, L is the active layer thickness, A is the area of the laser spot, β is the two-body recombination coefficient, and $t_{1/2}$ is the recombination time. Given that the 35 nm light penetration depth[56] is smaller than the 190 nm active layer thickness considered here ($\alpha L \gg 1$), the upper limit of integration can be extended to infinity:

$$Q_j = e{\cdot}A{\cdot}\int_0^\infty \{p_j(x, 0) + n_j(x, 0) - \beta{\cdot}t_{1/2}{\cdot} p_j(x, 0)n_j(x, 0)\}\,dx \tag{17}$$

While the coupled equations can be solved numerically by finite differencing,[18,19] the present simplified approach captures the initial burst of recombination by subtracting the annihilated carrier population in a single step. Combining eqs 9−17 yields

$$\begin{aligned} Q_j &= e{\cdot}A{\cdot}\int_0^\infty \{(p_0 + n_0)\exp(-\alpha x) - \beta t_{1/2} p_0 n_0 \exp(-2\alpha x)\}\,dx \\ &= e{\cdot}A\left\{\frac{(p_0 + n_0)}{\alpha} - \frac{\beta t_{1/2} p_0 n_0}{2\alpha}\right\} \\ &= \frac{3{\cdot}e{\cdot}f{\cdot}A}{2\hbar\omega} \end{aligned} \tag{18}$$

For applications involving color-tunable light sources, it should be noted that the collected charge Q_j is independent of the absorption coefficient in eq 18 due to the limiting condition $\alpha L \gg 1$.

Similarly, the amount of charge generated with both pulses incident on the device can be written using one-sided exponential carrier density profiles:

$$Q_{1+2}(\tau) = Q_1 + Q_2 - e{\cdot}\beta{\cdot}A{\cdot}R(\tau)\left\{\int_0^\infty p_1(x, \tau)n_2(x, 0)\,dx + \int_0^\infty n_1(x, \tau)p_2(x, 0)\,dx\right\} \tag{19}$$

As in eq 17, the upper limit of integration is extended to infinity under the assumption that the light penetration depth is much shorter than the active layer thickness ($\alpha L \gg 1$). The delay-dependent recombination time is given by

$$R(\tau) = \frac{1}{\beta\sqrt{p_0 n_0 \exp[-\alpha x_d(\tau)]}} \tag{20}$$

Integrating eq 19 over position yields

$$Q_{1+2}(\tau) = Q_1 + Q_2 - 2\beta{\cdot}p_0{\cdot}n_0{\cdot}V(\tau){\cdot}R(\tau) \tag{21}$$

where we have introduced the volume of overlapping carrier densities:

$$V(\tau) = \frac{eA}{2\alpha}\exp[-\alpha x_d(\tau)] \tag{22}$$

With the above definitions, the response of a photovoltaic cell to an individual laser beam (see eq 18) can be rewritten as

$$Q_j = 2(p_0 + n_0)V(0) - \beta p_0 n_0 V(0)R(0) \tag{23}$$

The overall NLPC signal is calculated by subtracting Q_1 and Q_2 from the total amount of charge collected when both laser pulses are incident on the device:

$$\Delta Q_{NLPC}(\tau) = Q_{1+2}(\tau) - Q_1 - Q_2 = -2\beta p_0 n_0 V(\tau)R(\tau) \tag{24}$$

This expression shows that the NLPC signal directly reflects the extent of spatial overlap between independently generated carrier populations, linking the observed device saturation to the underlying transport dynamics.

4. RESULTS AND DISCUSSION

The experiments presented in this section vary both the laser fluence and the delay time to confirm that the NLPC signal

https://doi.org/10.1021/acs.jpcc.5c05484
J. Phys. Chem. C XXXX, XXX, XXX−XXX

generation mechanism originates from two-body recombination processes involving independently excited carriers. In addition, the model developed in Section 3 is applied to extract drift velocities by simultaneously fitting the signals as functions of the two variables. We also address the broader question of how NLPC-type experiments based on alternative nonlinearities can be used to probe carrier transport phenomena with an emphasis on resolving quantitative signatures of carrier drift on nanosecond time scales.

4.1. Dynamics in NLPC Saturation Curves. The experimental data presented in Figure 4a were acquired

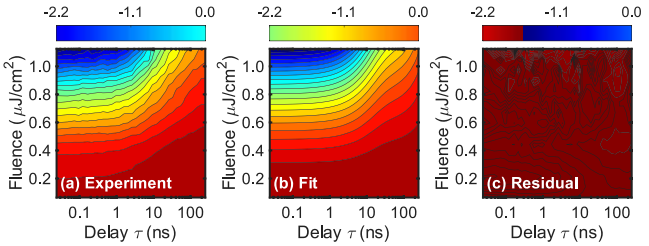

Figure 4. NLPC signals measured while simultaneously varying the fluences of both laser pulses. The (a) experimental data are in good agreement with (b) the fit calculated using eq 24, where (c) the residuals are less than 5% of the signal magnitude. The signal is expressed in units of pC. These data represent the average of five separate experiments.

while simultaneously varying the fluences of both laser pulses from 0.18 to 1.2 μJ/cm^2. As the delay time increases, the carriers generated by the first pulse drift out of the region subsequently excited by the second, reducing the device saturation. The small residual obtained when fitting the signal with eq 24 reflects the nonlinear scaling of the signal with laser fluence, confirming that the signal is dominated by two-body recombination processes involving carriers excited by separate laser pulses. Although the signals shown in Figure 4 represent averages over five independent experiments conducted on different electrodes and devices, each data set has been independently fitted to extract the mean values and standard deviations of the parameters listed in Table 2 (see Supporting Information). The mean drift velocity decreases from 6.22 to 0.26 m/s due to trap-induced dispersion on the 12.9 ns time scale. While the magnitude of drift velocity dispersion is sensitive to fabrication conditions, our present findings are consistent with previously observed initial velocities of 1−20 m/s and trapping times of 5−15 ns in $MAPbI_3$ photovoltaic cells.[18,19]

Table 2. Mean NLPC Fitting Parameters and Standard Deviations Across Devices

Parameter[a]	Fitted Value
v_{free}	6.22 ± 1.93 m/s
v_{trap}	0.26 ± 0.08 m/s
t_{trap}	12.88 ± 3.09 ns

[a]Uncertainty ranges represent standard deviations for five separate experiments (see Supporting Information).

The variances of the three fitting parameters are displayed on the diagonal of Table 3, whereas the off-diagonal entries correspond to the covariances between different parameters. The covariance matrix elements are further converted into unitless correlation coefficients by using normalization by the product of the parameter standard deviations. This correlation analysis shows a strong negative coupling between the free-carrier velocity and the trapping time (r = −0.73), a moderate negative coupling between trapped velocity and trapping time (r = −0.65), and a mild positive coupling between free and trapped velocities (r = +0.36). Practically, this means that the fit can trade a slightly faster initial drift for a slightly shorter trapping time (and vice versa) while still describing the data well. Consequently, the standard deviations reported across data sets in Table 2 reflect both true experimental variability among devices and correlation-induced interdependence of the fitted parameters within the model.

Table 3. Covariance and Correlation Matrices for NLPC Fit Parameters[a]

Parameters	v_{free} (m/s)	v_{trap} (m/s)	t_{trap} (ns)
v_{free} (m/s)	0.0183 (1.00)	0.0010 (0.36)	−0.0642 (−0.73)
v_{trap} (m/s)	0.0010 (0.36)	0.00045 (1.00)	−0.0090 (−0.65)
t_{trap} (ns)	−0.0642 (−0.73)	−0.0090 (−0.65)	0.4266 (1.00)

[a]Numbers outside parentheses represent covariances (with physical units determined by the parameter pair). Numbers inside parentheses are the corresponding unitless correlation coefficients.

To further demonstrate the behavior predicted by eq 24, the control experiments presented in Figure 5a−c show that the signals scale linearly with the fluences of the individual laser pulses, whereas nonlinear curvature is induced when the fluences of both pulses are varied simultaneously. Additionally, the slices of the fitted experimental data displayed in Figure 5d−f confirm good agreement with the calculated signals (red lines). While the percent deviations are generally larger at lower fluences, the signal magnitude rapidly diminishes with decreasing carrier densities and falls below the detection threshold of 0.1 μJ cm^{-2}. Accordingly, we do not draw firm quantitative conclusions from the larger relative deviations at the lowest fluences. The degree of device saturation is consistent with a two-body recombination coefficient of β =

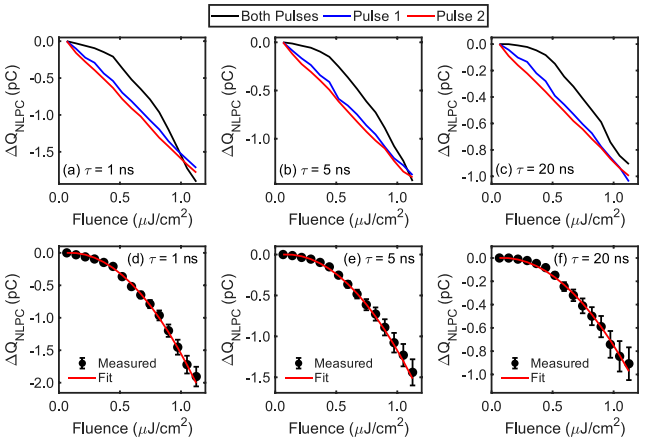

Figure 5. Measured NLPC signal profiles confirm two-body recombination processes. (a−c) The signal magnitudes scale linearly with the fluences of pulse 1 (blue) and pulse 2 (red), whereas the saturation curves exhibit nonlinear shapes when both pulses are varied simultaneously (black). (d−f) NLPC signals acquired while simultaneously varying the fluences of both laser pulses are overlaid with the global fit of the data shown in Figure 4. The uncertainty ranges represent standard deviations computed for five separate experiments.

https://doi.org/10.1021/acs.jpcc.5c05484
J. Phys. Chem. C XXXX, XXX, XXX−XXX

1.4×10^{-8} cm^3/s, which is within the range of recombination parameters reported for $MAPbI_3$ using alternate experimental methods ($0.8-20 \times 10^{-9}$ cm^3/s).[62−67] The observed signal curvature supports the applicability of our model for extracting carrier drift velocities and indicates that contributions from Auger processes involving mobile carriers are minimal within this range of laser fluences.

4.2. Implications for NLPC Detection Methods. In principle, the time-of-flight information targeted in the present work can be obtained using either recombination-induced or fourth-order perturbative NLPC-like techniques,[2−4,9,12−14] although distinctions between the two approaches have not been previously examined in the context of nanosecond transport mechanisms. To compare fundamental differences in the two classes of nonlinearities, we next translate the perturbative signal-generation mechanism into the framework of the present model, assuming that fourth-order photocurrent spectroscopy is conducted under the same experimental conditions as those used in this work.

Drawing inspiration from prior descriptions of action spectroscopies,[3,68,69] the fourth-order perturbative signal with photocurrent detection can be written at low optical density in the following form:

$$S^{(4)}_{\mathrm{pert}}(\tau) \propto \sum_j \Phi_j \sigma_j(\omega_1, \tau, \omega_2) I_1(\omega_1) I_2(\omega_2) \tag{25}$$

where Φ_j is the efficiency of the action signal generation mechanism for term j in the nonlinear response function and $I_m(\omega_m)$ is the intensity of laser pulse m. The susceptibility $\sigma_j(\omega_1,\tau,\omega_2)$ is written with variables representing the frequencies of the first and second laser pulses as well as the experimentally controlled delay time. With similar motivation, transient absorption signals are commonly expressed as functions of the excitation frequencies and delay time under the assumption that the laser pulse durations are long compared to the inverse of the spectroscopic line width.[70] In this limit, the laser is monochromatic with respect to electronic dephasing but still capable of resolving slower processes, such as carrier transport. More generally, the nonlinear optical response functions are convolved with the envelopes of the laser pulses for studies of femtosecond dynamics; however, this is unnecessary when using picosecond light sources.

To resolve drift velocities, time-of-flight techniques require localization of the carrier density near the transparent electrode through high optical densities.[26,27] Therefore, the expression for the signal must be integrated over the position within the active layer:

$$S^{(4)}_{\mathrm{pert}}(\omega_1, \tau, \omega_2) \propto \sum_j \Phi_j \int_0^\infty \sigma_j(\omega_1, \tau, \omega_2, x) I_1(x, \omega_1) I_2(x, \omega_2)\, \mathrm{d}x \tag{26}$$

Here, the light intensity varies with x, and the upper limit of the integral is set to infinity assuming that $\alpha L \ll 1$. The susceptibility $\sigma_j(\omega_1, \tau, \omega_2, x)$ may also vary with position x if the electrons and holes have distinct resonances. Since the objective is to capture time-of-flight signatures rather than to isolate individual nonlinear contributions, the summation over terms in the response is replaced by a total cross section representing the combined response at the pump and probe frequencies (ω_1 and ω_2):

$$S^{(4)}_{\mathrm{pert}}(\omega_1, \tau, \omega_2) \propto \int_0^\infty \sigma_{\mathrm{total}}(\omega_1, \tau, \omega_2, x) I_1(x, \omega_1) I_2(x, \omega_2)\, \mathrm{d}x \tag{27}$$

The integrand can be written as

$$\sigma_{\mathrm{total}}(\omega_1, \tau, \omega_2, x) I_1(x, \omega_1) I_2(x, \omega_2) \propto [\alpha_p^*(\omega_2) p_1(x, \tau, \omega_1) + \alpha_n^*(\omega_2) n_1(x, \tau, \omega_1)] \times \exp[-\alpha(\omega_2) x] \tag{28}$$

where α_p^* (α_n^*) denote the absorbance coefficients for the photoexcited holes and electrons, respectively, and the carrier densities excited by the first pulse are given in eqs 14 and 15.

The above expressions have been written with explicit pump and probe frequencies; however, we now omit the frequency variables for the laser pulses and consider the present special case of narrowband, single-color excitation. In this simplified notation, the expression for the fourth-order signal can be written as the following proportionality:

$$S^{(4)}_{\mathrm{pert}}(\tau) \propto p_0 \alpha_p^* \int_0^\infty \exp[-2\alpha x - \alpha x_{\mathrm{d}}(\tau)]\, \mathrm{d}x + n_0 \alpha_n^* \int_{x_{\mathrm{d}}(\tau)}^\infty \exp[-2\alpha x + \alpha x_{\mathrm{d}}(\tau)]\, \mathrm{d}x \tag{29}$$

Evaluation of the integrals over the position within the active layer yields

$$S^{(4)}_{\mathrm{pert}}(\tau) \propto (p_0 \alpha_p^* + n_0 \alpha_n^*) V(\tau) \tag{30}$$

where the volume of density overlap $V(\tau)$ is defined in eq 22.

With the goal of comparing time-of-flight signatures for the two detection methods, the scaling of the recombination-induced signal with the absorption coefficient and location of the charge distribution excited by the first laser pulse is expressed as

$$\Delta Q_{\mathrm{NLPC}}(\tau) \propto \exp[-\alpha x_{\mathrm{d}}(\tau)/2] \tag{31}$$

while the corresponding fourth-order perturbative signal is given by

$$S^{(4)}_{\mathrm{pert}}(\tau) \propto (\alpha_p^* + \alpha_n^*) \exp[-\alpha x_{\mathrm{d}}(\tau)] \tag{32}$$

The signals associated with both detection processes decay exponentially as the carriers excited by the first laser pulse drift away from the ITO contact, although the NLPC signal decays 50% more slowly. This comparison suggests that the two experimental methods provide the same time-of-flight information when recombination is faster than carrier transit across the photoexcited region of the active layer, $R(\tau) \ll \alpha^{-1} v_d^{-1}(\tau)$. This condition is satisfied for nanosecond carrier transport in $MAPbI_3$ films under low-bias conditions, although studies of carrier drift in perovskite crystals under large external biases would likely require the pulse-width-limited time resolution available from fourth-order perturbative techniques. Because recombination-induced nonlinear responses carry the same dynamical information as the corresponding fourth-order process, the relationship between signals is distinct from the cascaded lower-order optical responses observed in off-resonant 2D Raman spectroscopies.[30−32]

Similarly, 2D NLPC spectra obtained by tuning the colors of narrowband pulses have been used to study charge funneling in layered perovskite devices containing mixed quantum-well phases.[21,22] In the recombination-induced approach, the

https://doi.org/10.1021/acs.jpcc.5c05484
J. Phys. Chem. C XXXX, XXX, XXX−XXX

populations of the separate phases are reflected by ground-state excitonic resonances, which are broadened by saturation processes;[17] however, the peak patterns in the 2D spectra closely resemble the features observed in 2D electronic spectroscopies applied to photosynthetic light harvesting systems.[71−75] These effects have been discussed for recombination-induced 2D spectra with fluorescence detection and can be directly extended to NLPC measurements.[17]

5. CONCLUDING REMARKS

In summary, the observed nonlinear scaling of NLPC signals with laser fluence demonstrates that the recombination-induced response arises from two-body recombination between carriers excited by separate laser pulses. While this fundamental aspect of the signal generation mechanism had previously been inferred through standalone control experiments, the present implementation of the NLPC method enables simultaneous characterization of the recombination-induced nonlinearity and detection of charge transport. The measured drift velocities are in good agreement with those found in prior work on $MAPbI_3$ photovoltaic cells using alternative measurement techniques.[17,18] The simplified model used to fit the experimental data retains the key physical behaviors captured by more detailed approaches while remaining more practical for signal interpretation. This modeling framework can be extended to capture the time-of-flight information provided by NLPC-type experiments based on either recombination-induced or fourth-order perturbative responses. Our analysis suggests that the two experimental methods have similar sensitivities to long-range carrier transport on nanosecond time scales in thin-film devices; however, the fourth-order approach is uniquely equipped for studies of femtosecond dynamics due to its pulse width-limited time resolution.

■ ASSOCIATED CONTENT

Supporting Information

The Supporting Information is available free of charge at https://pubs.acs.org/doi/10.1021/acs.jpcc.5c05484.

Five separate experimental data sets, along with plots of the signal components used to define the nonlinearity (Q_1, Q_1, and Q_{1+2}), temporal profiles of the NLPC signals, a summary of the multiple-trapping model used to compute the carrier densities shown in Figure 3a−c, and the derivation of eq 7 (PDF)

■ AUTHOR INFORMATION

Corresponding Author

Andrew M. Moran − *Department of Chemistry, University of North Carolina at Chapel Hill, Chapel Hill, North Carolina 27599, United States;* orcid.org/0000-0001-7761-7613; Email: ammoran@unc.edu

Authors

Saba Mahmoodpour − *Department of Chemistry, University of North Carolina at Chapel Hill, Chapel Hill, North Carolina 27599, United States;* orcid.org/0000-0002-5036-7092

Zijian Gan − *Department of Chemistry, University of North Carolina at Chapel Hill, Chapel Hill, North Carolina 27599, United States;* orcid.org/0000-0002-3751-5249

Liang Yan − *Department of Chemistry, University of North Carolina at Chapel Hill, Chapel Hill, North Carolina 27599, United States;* orcid.org/0000-0003-4122-7466

Wei You − *Department of Chemistry, University of North Carolina at Chapel Hill, Chapel Hill, North Carolina 27599, United States;* orcid.org/0000-0003-0354-1948

Complete contact information is available at: https://pubs.acs.org/10.1021/acs.jpcc.5c05484

Notes

The authors declare no competing financial interest.

■ ACKNOWLEDGMENTS

This work is supported by the National Science Foundation under CHE-2247159 (S.M., Z.G., and A.M.M.) and CHE-2154791 (L.Y. and W.Y.). This work was performed in part at the Chapel Hill Analytical and Nanofabrication Laboratory, CHANL, a member of the North Carolina Research Triangle Nanotechnology Network, RTNN, which is supported by the National Science Foundation, Grant ECCS-2025064, as part of the National Nanotechnology Coordinated Infrastructure, NNCI.

■ REFERENCES

(1) Tekavec, P. F.; Lott, G. A.; Marcus, A. H. Fluorescence-detected two-dimensional electronic coherence spectroscopy by acousto-optic phase modulation. *J. Chem. Phys.* **2007**, *127* (21), No. 214307.

(2) Nardin, G.; Autry, T. M.; Silverman, K. L.; Cundiff, S. T. Multidimensional coherent photocurrent spectroscopy of a semiconductor nanostructure. *Opt. Express* **2013**, *21* (23), 28617−28627.

(3) Karki, K. J.; Widom, J. R.; Seibt, J.; Moody, I.; Lonergan, M. C.; Pullerits, T.; Marcus, A. H. Coherent two-dimensional photocurrent spectroscopy in a PbS quantum dot photocell. *Nat. Commun.* **2014**, *5* (1), 5869.

(4) Bakulin, A. A.; Silva, C.; Vella, E. Ultrafast Spectroscopy with Photocurrent Detection: Watching Excitonic Optoelectronic Systems at Work. *J. Phys. Chem. Lett.* **2016**, *7* (2), 250−258.

(5) Mueller, S.; Brixner, T. Molecular Coherent Three-Quantum Two-Dimensional Fluorescence Spectroscopy. *J. Phys. Chem. Lett.* **2020**, *11* (13), 5139−5147.

(6) Agathangelou, D.; Javed, A.; Sessa, F.; Solinas, X.; Joffre, M.; Ogilvie, J. P. Phase-modulated rapid-scanning fluorescence-detected two-dimensional electronic spectroscopy. *J. Chem. Phys.* **2021**, *155* (9), No. 094201.

(7) Wang, C.; Ali, A.; Karki, K. J. Multiphoton photocurrent in wide bandgap semiconductors for nonlinear optoelectronics: Comparison of GaP, GaN/InGaN, and SiC. *Appl. Phys. Lett.* **2024**, *124* (6), No. 062101.

(8) López-Ortiz, M.; Bolzonello, L.; Bruschi, M.; Fresch, E.; Collini, E.; Hu, C.; Croce, R.; van Hulst, N. F.; Gorostiza, P. Photoelectrochemical Two-Dimensional Electronic Spectroscopy (PEC2DES) of Photosystem I: Charge Separation Dynamics Hidden in a Multichromophoric Landscape. *ACS Appl. Mater. Interfaces.* **2024**, *16* (33), 43451−43461.

(9) Faitz, Z. M.; Im, D.; Blackwell, C. J.; Arnold, M. S.; Zanni, M. T. A spectrometer design that eliminates incoherent mixing signals in 2D action spectroscopies. *J. Chem. Phys.* **2024**, *161* (13), No. 134202.

(10) Xie, Q.; Xu, X. G. Action-based two-dimensional infrared spectroscopy on the horizon. *J. Chem. Phys.* **2025**, *162* (10), No. 100901.

(11) Hao, H.; Malý, P.; Cui, Y.; Binzer, M.; Thyrhaug, E.; Hauer, J. Fluorescence-Detected Pump−Probe Spectroscopy for Artifact-Free Detection of Stokes Shift Dynamics. *J. Phys. Chem. Lett.* **2025**, *16* (20), 4861−4868.

(12) Vella, E.; Li, H.; Grégoire, P.; Tuladhar, S. M.; Vezie, M. S.; Few, S.; Bazán, C. M.; Nelson, J.; Silva-Acuña, C.; Bittner, E. R.

Ultrafast decoherence dynamics govern photocarrier generation efficiencies in polymer solar cells. *Sci. Rep.* **2016**, *6* (1), 29437.
(13) Damtie, F. A.; Wacker, A.; Pullerits, T.; Karki, K. J. Two-dimensional action spectroscopy of excitonic systems: Explicit simulation using a phase-modulation technique. *Phys. Rev. A* **2017**, *96* (5), No. 053830.
(14) Bolzonello, L.; Bernal-Texca, F.; Gerling, L. G.; Ockova, J.; Collini, E.; Martorell, J.; van Hulst, N. F. Photocurrent-Detected 2D Electronic Spectroscopy Reveals Ultrafast Hole Transfer in Operating PM6/Y6 Organic Solar Cells. *J. Phys. Chem. Lett.* **2021**, *12* (16), 3983−3988.
(15) Rojas-Gatjens, E.; Yallum, K. M.; Shi, Y.; Zheng, Y.; Bills, T.; Perini, C. A. R.; Correa-Baena, J.-P.; Ginger, D. S.; Banerji, N.; Silva-Acuña, C. Resolving Nonlinear Recombination Dynamics in Semiconductors via Ultrafast Excitation Correlation Spectroscopy: Photoluminescence versus Photocurrent Detection. *J. Phys. Chem. C* **2023**, *127* (32), 15969−15977.
(16) Wang, C.; Ali, A.; Wu, J.; Huang, W.; Lu, H.; Karki, K. J. Effects of impurity band on multiphoton photocurrent in GaN and InGaN photodetectors. *Opt. Mater.* **2024**, *149*, No. 114986.
(17) McNamee, M. G.; Ouyang, Z.; Yan, L.; Gan, Z.; Zhou, N.; Williams, O. F.; You, W.; Moran, A. M. Uncovering Transport Mechanisms in Perovskite Materials and Devices with Recombination-Induced Action Spectroscopies. *J. Phys. Chem. C* **2023**, *127* (6), 2782−2791.
(18) Ouyang, Z.; Yan, L.; You, W.; Moran, A. M. Probing drift velocity dispersion in MAPbI3 photovoltaic cells with nonlinear photocurrent spectroscopy. *J. Chem. Phys.* **2022**, *157* (17), No. 174202.
(19) Ouyang, Z.; Zhou, N.; McNamee, M. G.; Yan, L.; Williams, O. F.; Gan, Z.; Gao, R.; You, W.; Moran, A. M. Origin of layered perovskite device efficiencies revealed by multidimensional time-of-flight spectroscopy. *J. Chem. Phys.* **2022**, *156* (8), No. 084202.
(20) Zhou, N.; Ouyang, Z.; Yan, L.; McNamee, M. G.; You, W.; Moran, A. M. Elucidation of Quantum-Well-Specific Carrier Mobilities in Layered Perovskites. *J. Phys. Chem. Lett.* **2021**, *12* (4), 1116−1123.
(21) Ouyang, Z.; Zhou, N.; McNamee, M. G.; Yan, L.; Williams, O. F.; You, W.; Moran, A. M. Multidimensional time-of-flight spectroscopy. *J. Chem. Phys.* **2021**, *154* (22), No. 220901.
(22) Zhou, N.; Ouyang, Z.; Hu, J.; Williams, O. F.; Yan, L.; You, W.; Moran, A. M. Distinguishing Energy- and Charge-Transfer Processes in Layered Perovskite Quantum Wells with Two-Dimensional Action Spectroscopies. *J. Phys. Chem. Lett.* **2020**, *11* (12), 4570−4577.
(23) Ouyang, Z.; Gan, Z.; Yan, L.; You, W.; Moran, A. M. Measuring carrier diffusion in MAPbI3 solar cells with photocurrent-detected transient grating spectroscopy. *J. Chem. Phys.* **2023**, *159* (9), No. 094201.
(24) Gan, Z.; Mahmoodpour, S.; Gloor, C. J.; Feng, S.; Yan, L.; You, W.; Moran, A. M. Resolving dispersive diffusion in layered perovskites with photocurrent-detected transient gratings. *J. Chem. Phys.* **2025**, *162* (7), No. 074201.
(25) Bruschi, M.; Bolzonello, L.; Gallina, F.; Fresch, B. Unifying Nonlinear Response and Incoherent Mixing in Action-2D Electronic Spectroscopy. *J. Phys. Chem. Lett.* **2023**, *14* (30), 6872−6879.
(26) Bronger, T. Time-of-Flight Analysis. In *Advanced Characterization Techniques for Thin Film Solar Cells*; Abou-Ras, D., Kirchartz, T., Rau, U.,, Eds.; Wiley-VCH: Weinheim, 1991; Vol. *1*, pp 121−145.
(27) Karl, N. Charge-Carrier Mobility in Organic Crystals. In *Organic Electronic Materials Conjugated Polymers and Low Molecular Weight Organic Solids*; Farchoni, R., Grosso, G.,, Eds.; Springer-Verlag: New York, 2001.
(28) Ivanecky, J. E.; Wright, J. C. An investigation of the origins and efficiencies of higher-order nonlinear spectroscopic processes. *Chem. Phys. Lett.* **1993**, *206* (5), 437−444.
(29) Ulness, D. J.; Kirkwood, J. C.; Albrecht, A. C. Competitive events in fifth order time resolved coherent Raman scattering: Direct versus sequential processes. *J. Chem. Phys.* **1998**, *108* (10), 3897−3902.
(30) Blank, D. A.; Kaufman, L. J.; Fleming, G. R. Fifth-order two-dimensional Raman spectra of CS2 are dominated by third-order cascades. *J. Chem. Phys.* **1999**, *111* (7), 3105−3114.
(31) Kubarych, K. J.; Milne, C. J.; Lin, S.; Astinov, V.; Miller, R. J. D. Diffractive optics-based six-wave mixing: Heterodyne detection of the full $\chi(5)$ tensor of liquid CS2. *J. Chem. Phys.* **2002**, *116* (5), 2016−2042.
(32) Wilson, K. C.; Lyons, B.; Mehlenbacher, R.; Sabatini, R.; McCamant, D. W. Two-dimensional femtosecond stimulated Raman spectroscopy: Observation of cascading Raman signals in acetonitrile. *J. Chem. Phys.* **2009**, *131* (21), No. 214502.
(33) Grégoire, P.; Srimath Kandada, A. R.; Vella, E.; Tao, C.; Leonelli, R.; Silva, C. Incoherent population mixing contributions to phase-modulation two-dimensional coherent excitation spectra. *J. Chem. Phys.* **2017**, *147* (11), No. 114201.
(34) Kalaee, A. A. S.; Damtie, F.; Karki, K. J. Differentiation of True Nonlinear and Incoherent Mixing of Linear Signals in Action-Detected 2D Spectroscopy. *J. Phys. Chem. A* **2019**, *123* (19), 4119−4124.
(35) Kühn, O.; Mančal, T.; Pullerits, T. Interpreting Fluorescence Detected Two-Dimensional Electronic Spectroscopy. *J. Phys. Chem. Lett.* **2020**, *11* (3), 838−842.
(36) Bargigia, I.; Gutiérrez-Meza, E.; Valverde-Chávez, D. A.; Marques, S. R.; Srimath Kandada, A. R.; Silva, C. Identifying incoherent mixing effects in the coherent two-dimensional photocurrent excitation spectra of semiconductors. *J. Chem. Phys.* **2022**, *157* (20), No. 204202.
(37) Shockley, W.; Read, W. T. Statistics of the Recombinations of Holes and Electrons. *Phys. Rev.* **1952**, *87* (5), 835−842.
(38) Landsberg, P. T. *Recombination in Semiconductors*; Cambridge University Press: Cambridge, 1991.
(39) Tiedje, T. Time-Resolved Charge Transport in Hydrogenated Amorphous Silicon. In *The Physics of Hydrogenated Amorphous Silicon II: Electronic and Vibrational Properties*, Joannopoulos, J.; Lucovsky, G., Eds.; Springer: Berlin, 1984; Vol. *56*, pp 261−300.
(40) Tiedje, T.; Rose, A. A physical interpretation of dispersive transport in disordered semiconductors. *Solid State Commun.* **1981**, *37* (1), 49−52.
(41) Noolandi, J. Multiple-trapping model of anomalous transit-time dispersion in α-Se. *Phys. Rev. B* **1977**, *16* (10), 4466−4473.
(42) Schmidlin, F. W. Theory of trap-controlled transient photoconduction. *Phys. Rev. B* **1977**, *16* (6), 2362−2385.
(43) Silver, M.; Cohen, L. Monte Carlo simulation of anomalous transit-time dispersion of amorphous solids. *Phys. Rev. B* **1977**, *15* (6), 3276−3278.
(44) Scher, H.; Shlesinger, M. F.; Bendler, J. T. Time-Scale Invariance in Transport and Relaxation. *Phys. Today* **1991**, *44* (1), 26−34.
(45) Scher, H.; Montroll, E. W. Anomalous transit-time dispersion in amorphous solids. *Phys. Rev. B* **1975**, *12* (6), 2455−2477.
(46) Pfister, G.; Scher, H. Dispersive (non-Gaussian) transient transport in disordered solids. *Adv. Phys.* **1978**, *27* (5), 747−798.
(47) Arkhipov, V. I.; Rudenko, A. I. Drift and diffusion in materials with traps. *Philos. Mag. B* **1982**, *45* (2), 189−207.
(48) Wright, A. D.; Milot, R. L.; Eperon, G. E.; Snaith, H. J.; Johnston, M. B.; Herz, L. M. Band-Tail Recombination in Hybrid Lead Iodide Perovskite. *Adv. Funct. Mater.* **2017**, *27* (29), No. 1700860.
(49) Fu, X.; Weber, K. J.; White, T. P. Characterization of trap states in perovskite films by simultaneous fitting of steady-state and transient photoluminescence measurements. *J. Appl. Phys.* **2018**, *124* (7), No. 073102.
(50) Zhou, Y.; Zhang, H.; Xian, Y.; Shi, Z.; Aboa, J. N.; Fei, C.; Yang, G.; Li, N.; Selim, F. A.; Yan, Y.; et al. Enhancing charge-emitting shallow traps in metal halide perovskites by > 100 times by surface strain. *Joule* **2025**, *9* (1), No. 101772.
(51) Baumann, A.; Väth, S.; Rieder, P.; Heiber, M. C.; Tvingstedt, K.; Dyakonov, V. Identification of Trap States in Perovskite Solar Cells. *J. Phys. Chem. Lett.* **2015**, *6* (12), 2350−2354.

https://doi.org/10.1021/acs.jpcc.5c05484
J. Phys. Chem. C XXXX, XXX, XXX−XXX

(52) Wu, X.; Trinh, M. T.; Niesner, D.; Zhu, H.; Norman, Z.; Owen, J. S.; Yaffe, O.; Kudisch, B. J.; Zhu, X. Y. Trap States in Lead Iodide Perovskites. *J. Am. Chem. Soc.* **2015**, *137* (5), 2089−2096.
(53) Musiienko, A.; Pipek, J.; Praus, P.; Brynza, M.; Belas, E.; Dryzhakov, B.; Du, M.-H.; Ahmadi, M.; Grill, R. Deciphering the effect of traps on electronic charge transport properties of methylammonium lead tribromide perovskite. *Sci. Adv.* **2020**, *6* (37), No. eabb6393.
(54) Telser, L. G. The Lognormal Distribution, J. Aitchison and J. A. C. Brown, Cambridge, England: Cambridge University Press, 1957, Pp. xviii, 176. $6.50. *American Journal of Agricultural Economics* **1959**, *41* (1), 161−162.
(55) Spear, W. E. Drift mobility techniques for the study of electrical transport properties in insulating solids. *J. Non-Cryst. Solids* **1969**, *1* (3), 197−214.
(56) Löper, P.; Stuckelberger, M.; Niesen, B.; Werner, J.; Filipič, M.; Moon, S.-J.; Yum, J.-H.; Topič, M.; De Wolf, S.; Ballif, C. Complex Refractive Index Spectra of CH3NH3PbI3 Perovskite Thin Films Determined by Spectroscopic Ellipsometry and Spectrophotometry. *J. Phys. Chem. Lett.* **2015**, *6* (1), 66−71.
(57) Williams, O. F.; Zhou, N.; Hu, J.; Ouyang, Z.; Kumbhar, A.; You, W.; Moran, A. M. Imaging Excited State Dynamics in Layered 2D Perovskites with Transient Absorption Microscopy. *J. Phys. Chem. A* **2019**, *123* (51), 11012−11021.
(58) Heo, S.; Seo, G.; Lee, Y.; Lee, D.; Seol, M.; Lee, J.; Park, J.-B.; Kim, K.; Yun, D.-J.; Kim, Y. S.; et al. Deep level trapped defect analysis in CH3NH3PbI3 perovskite solar cells by deep level transient spectroscopy. *Energy Environ. Sci.* **2017**, *10* (5), 1128−1133.
(59) Duijnstee, E. A.; Le Corre, V. M.; Johnston, M. B.; Koster, L. J. A.; Lim, J.; Snaith, H. J. Understanding Dark Current-Voltage Characteristics in Metal-Halide Perovskite Single Crystals. *Physical Review Applied* **2021**, *15* (1), No. 014006.
(60) Forde, A.; Kilin, D. Defect Tolerance Mechanism Revealed! Influence of Polaron Occupied Surface Trap States on CsPbBr3 Nanocrystal Photoluminescence: Ab Initio Excited-State Dynamics. *J. Chem. Theory Comput.* **2021**, *17* (11), 7224−7236.
(61) Wang, H.; Zhang, C.; Chan, W.; Tiwari, S.; Rana, F. Ultrafast response of monolayer molybdenum disulfide photodetectors. *Nat. Commun.* **2015**, *6* (1), 8831.
(62) Savenije, T. J.; Ponseca, C. S.; Kunneman, L.; Abdellah, M.; Zheng, K.; Tian, Y.; Zhu, Q.; Canton, S. E.; Scheblykin, I. G.; Pullerits, T.; et al. Thermally Activated Exciton Dissociation and Recombination Control the Carrier Dynamics in Organometal Halide Perovskite. *J. Phys. Chem. Lett.* **2014**, *5* (13), 2189−2194.
(63) Yamada, Y.; Nakamura, T.; Endo, M.; Wakamiya, A.; Kanemitsu, Y. Photocarrier Recombination Dynamics in Perovskite CH3NH3PbI3 for Solar Cell Applications. *J. Am. Chem. Soc.* **2014**, *136* (33), 11610−11613.
(64) Manser, J. S.; Kamat, P. V. Band filling with free charge carriers in organometal halide perovskites. *Nat. Photonics* **2014**, *8* (9), 737−743.
(65) Guo, Z.; Manser, J. S.; Wan, Y.; Kamat, P. V.; Huang, L. Spatial and temporal imaging of long-range charge transport in perovskite thin films by ultrafast microscopy. *Nat. Commun.* **2015**, *6* (1), 7471.
(66) D'Innocenzo, V.; Srimath Kandada, A. R.; De Bastiani, M.; Gandini, M.; Petrozza, A. Tuning the Light Emission Properties by Band Gap Engineering in Hybrid Lead Halide Perovskite. *J. Am. Chem. Soc.* **2014**, *136* (51), 17730−17733.
(67) Herz, L. M. Charge-Carrier Dynamics in Organic-Inorganic Metal Halide Perovskites. *Annu. Rev. Phys. Chem.* **2016**, *67* (1), 65−89.
(68) Kunsel, T.; Tiwari, V.; Matutes, Y. A.; Gardiner, A. T.; Cogdell, R. J.; Ogilvie, J. P.; Jansen, T. L. C. Simulating Fluorescence-Detected Two-Dimensional Electronic Spectroscopy of Multichromophoric Systems. *J. Phys. Chem. B* **2019**, *123* (2), 394−406.
(69) Charvátová, K.; Malý, P. Spectro-temporal symmetry in action-detected optical spectroscopy: Highlighting excited-state dynamics in large systems. *J. Chem. Phys.* **2025**, *162* (12), No. 124204.
(70) Mukamel, S. *Principles of Nonlinear Optical Spectroscopy*; Oxford University Press: New York, 1995.
(71) Irgen-Gioro, S.; Gururangan, K.; Spencer, A. P.; Harel, E. Non-Uniform Excited State Electronic-Vibrational Coupling of Pigment−Protein Complexes. *J. Phys. Chem. Lett.* **2020**, *11* (24), 10388−10395.
(72) Song, Y.; Sechrist, R.; Nguyen, H. H.; Johnson, W.; Abramavicius, D.; Redding, K. E.; Ogilvie, J. P. Excitonic structure and charge separation in the heliobacterial reaction center probed by multispectral multidimensional spectroscopy. *Nat. Commun.* **2021**, *12* (1), 2801.
(73) Higgins, J. S.; Lloyd, L. T.; Sohail, S. H.; Allodi, M. A.; Otto, J. P.; Saer, R. G.; Wood, R. E.; Massey, S. C.; Ting, P.-C.; Blankenship, R. E.; et al. Photosynthesis tunes quantum-mechanical mixing of electronic and vibrational states to steer exciton energy transfer. *Proc. Natl. Acad. Sci. U.S.A.* **2021**, *118* (11), No. e2018240118.
(74) Sil, S.; Tilluck, R. W.; Mohan T. M., N.; Leslie, C. H.; Rose, J. B.; Domínguez-Martín, M. A.; Lou, W.; Kerfeld, C. A.; Beck, W. F. Excitation energy transfer and vibronic coherence in intact phycobilisomes. *Nat. Chem.* **2022**, *14* (11), 1286−1294.
(75) Fleming, G. R.; Scholes, G. D. The development and applications of multidimensional biomolecular spectroscopy illustrated by photosynthetic light harvesting. *Q. Rev. Biophys.* **2024**, *57*, No. e11.

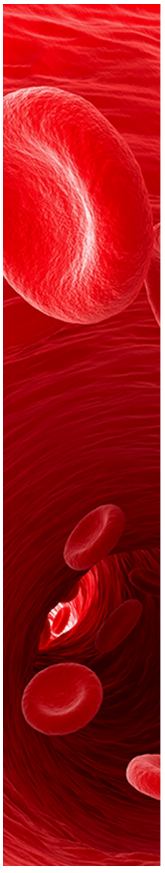
CAS BIOFINDER DISCOVERY PLATFORM™
CAS BIOFINDER HELPS YOU FIND YOUR NEXT BREAKTHROUGH FASTER
Navigate pathways, targets, and diseases with precision
Explore CAS BioFinder
CAS
A division of the American Chemical Society

https://doi.org/10.1021/acs.jpcc.5c05484
J. Phys. Chem. C XXXX, XXX, XXX−XXX